Ceramics International 44 (2018) 14348–14354

Contents lists available at ScienceDirect

Ceramics International

journal homepage: www.elsevier.com/locate/ceramint

Influence of the porosity caused by incomplete sintering on the mechanical behaviour of lanthanum silicate oxyapatite

Ramiro J. Moreira Toja[a,*], Nicolás M. Rendtorff[a,b], Esteban F. Aglietti[a,b], Tetsuo Uchikoshi[c], Yoshio Sakka[c], Gustavo Suárez[a,b]

[a] Centro de Tecnología de Recursos Minerales y Cerámica (CETMIC), Camino Centenario y 506, M.B. Gonnet C.C.49 (B1897ZCA), Argentina
[b] Departamento de Química, Facultad de Ciencias Exactas, UNLP, Calle 115 y 47, La Plata 1900, Argentina
[c] National Institute for Materials Science (NIMS), Tsukuba, Ibaraki 305-0047, Japan

ARTICLE INFO

Keywords:
Lanthanum silicate oxyapatite
Mechanical properties
Young's modulus
Fracture

ABSTRACT

Lanthanum silicate oxyapatite (LSO) is an encouraging material for its use as an electrolyte in intermediate temperature solid oxide fuel cells. There is a vacancy in knowledge respecting to LSO's mechanical properties, and thus they are the scope of research of the present work.

Isostatically pressed bars were sintered at temperatures from 1200 °C to 1500 °C. The dependence of Young's modulus with porosity was fitted using three different modeling curves, and extrapolated for a fully dense material. The fitting of these equations give an E_0 between 144 GPa and 169 GPa. This is the first time that LSO's Young's modulus is reported.

Flexural strength,Vickers hardness, fracture toughness (K_{IC}) from microindentation cracks and nanohardness were also measured. Scanning electron micrography was performed on both a sub-sintered and the most sintered sample, and the microstructure and fracture mechanism were analyzed.

In general, the mechanical behaviour is similar to other intermediate temperature solid oxide electrolytes. The fracture mechanism of the most sintered sample makes it well-suited for future SOFC applications.

1. Introduction

Solid oxide fuel cells (SOFCs) are electrochemical energy-conversion devices, which have a long history of research, development and implementations since their inception in 1853 by Gaugain [1]. Nowadays, they are used for providing electric energy in specific situations that can't get connected to mains electricity distribution grid, such as military outposts or space vehicles. Although their peripheral use in present energetic infrastructure, they are promising candidates to replace combustion engines in energy conversion tasks, due to having a better performance as not being limited by Carnot's cycle.

In commercial SOFC systems based on oxygen conduction electrolytes, the most widely used ceramic electrolyte is yttria-stabilized zirconia (YSZ), favored by its high oxide ion conductivity at high temperatures (800–1000 °C). Nevertheless, there is a trend to switch to lower operation temperatures, in order to reduce operational costs, allow a broader set of materials (as seals and stack interconnections) to be used and overcome the low lifetime of the components caused by the high operation temperature [2–4],as well as making SOFCs more suitable for other uses in which high temperatures can't be tolerated, like domestic electricity generation and vehicle auxiliary power units [5]. Lanthanum silicate oxyapatite (LSO), with an apatite-like structure and formula $La_{9.33+x}(SiO_4)_6O_{2+3\times/2}$ (where $0 < x < 0.66$), is an encouraging material for replacing YSZ in intermediate temperature SOFCs (IT-SOFCs), i.e. in the range between 600 °C and 800 °C. Since Nakayama et al. [6] reported oxygen ion conductivity in rare earth silicate oxyapatites, it has become the focus of a vast amount of investigation [7–20]; recently, the possibility to confer proton conductivity to LSO has been investigated [21].

The design of SOFCs and SOFC stacks demands not only the knowledge of electric properties (e.g. area-specific resistivity, conduction mechanism) of its constituents, but also their mechanical properties and behaviour, in order to build devices able to operate for long terms [5,22]; these materials must possess adequate mechanical properties such as high hardness, rigidity and fracture toughness in order to assure a desirable performance of the anode-electrolyte-cathode final assembly [23]. Nevertheless, lanthanum silicates have been poorly studied in this aspect: mainly lanthanum silicate glasses [24,25] and lanthanum silicate oxyapatites doped with germanium [23].

In the present work we address the lack of information regarding the

* Corresponding author.
E-mail address: rmtoja@cetmic.unlp.edu.ar (R.J. Moreira Toja).

https://doi.org/10.1016/j.ceramint.2018.05.043
Received 24 April 2018; Received in revised form 4 May 2018; Accepted 6 May 2018
Available online 18 May 2018

mechanical properties of LSO. We investigate Young's modulus, hardness, fracture toughness and flexural strength in relation with the material's porosity, which in turn is controlled by the sintering temperature. Furthermore, we report for the first time lanthanum silicate oxyapatite's Young's modulus for different porosities, and extrapolate it for a fully dense material.

2. Materials and methods

2.1. Material

Synthesis of the LSO powder was carried out the same way as in a previous study [26]. In essence, $La(OH)_3$ and SiO_2 powders were mixed and calcined thrice at 1400 °C for 10 h in air. The synthesis process used to obtain the ceramic powder is described elsewhere [27].

2.2. Forming

Rectangular cross-section bar samples of approximately 5.6 g, with dimensions of 50 × 7 × 3 mm^3 each were uniaxially pressed at 50 MPa, grinded with mortar and uniaxially pressed at 50 MPa again, in order to avoid a preferential orientation that would lead to lamination. Then, the bars were isostatically pressed at 100 MPa for 5 min and dried at 110 °C for 24 h.

2.3. Sintering

Bars were sintered at temperatures of 1200, 1300, 1400 and 1500 °C, six bars at each temperature, in an electric furnace with heating rates of 5 °C/min and a dwell time of 2 h, in an air atmosphere. Samples sintered at each of these temperatures will be named through this work M12, M13, M14 and M15, respectively.

2.4. Sample characterizations

Density and porosity of sintered pieces were determined by Archimedes method, using distilled water.

A multi-technique approach was used to examine LSO mechanical properties. The impulse excitation method (Grindosonic MK05 “Industrial”) was employed to measure Young's modulus, following Eq. (1) [28]

$$E = 0.94642\frac{\rho l^4 f^2}{t^2}T \quad (1)$$

where ρ is the material's density, l is the length of the bar, f is the fundamental resonant frequency, t is the cross-sectional area of the beam and T a correction factor given by Spinner and Tefft [29]. Stress-strain curves from three point flexural tests (INSTRON 5985) were studied to obtain flexural strength. It is possible to evaluate Young's modulus from the slope of these stress-strain curves; however, this method is not recommended, as non-elastic contributions to the deflection render it an inaccurate measurement technique, with a lower precision and repeatability than other techniques [30,31]. Nanoindentation tests were performed on polished samples (down to 1 µm diamond paste followed by a 5 h polish in a Buehler Vibramet using a 50 nm alumina suspension) of an M15 sample using a nanoindenter (Hysitron Triboindenter TI 900) with a Berkovich diamond tip up to a 50 mN load with a loading/unloading rate of 10 mN/s and 2 s dwell at the maximum load. Reduced Young's modulus and hardness were calculated using the Oliver and Pharr model [32], averaging 25 nanoindentations. Fig. 1 shows a load vs displacement plot for one of the nanoindentations. Nanohardness is calculated using the maximum load (P_{max}) and a projected area ($A_p = 24.5\,h_{max}^2$), while the reduced Young's modulus is requires dP/dh and A_p. The Young's modulus of the material can be further calculated following the expression

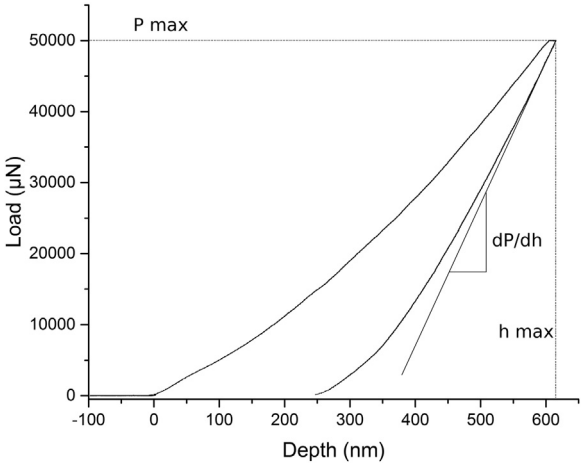

Fig. 1. nanoindenter load as a function of tip displacement.

$$\frac{1}{E_r} = \frac{1-\nu_s^2}{E_s} + \frac{1-\nu_i^2}{E_i} \quad (2)$$

where E_r is the reduced Young's modulus, E_s is the Young's modulus of the sample, E_i is the Young's modulus of the indenter, ν_s is the Poisson ratio of the sample and ν_i is the Poisson ratio of the indenter. For the diamond Berkovich indenter used, E_i and ν_i have values of 1140 GPa and 0.07 [33], respectively, while a value of 0.3 was used for ν_i.

Hardness of LSO samples was also measured by a Vickers hardness tester (Buehler Indentamet 1100) on surfaces polished down to 1 µm diamond paste. The load used was 0.3 kgf and the load time was 15 s. K_{IC} was calculated, when possible, via the Pamlqvist method, using the formula proposed by Lankford [34], shown in Eq. (3), which fits well for both Palmqvist and median cracks.

$$K_{IC} = 0.142(Ha^{0.5})\left(\frac{E\Phi}{H}\right)^{0.4}\frac{(c/a)^{-1.56}}{\Phi} \quad (3)$$

The microstructures of samples and cracks developed from microindentation were studied by scanning electron microscopy (FEI Quanta200) on fracture surfaces and polished surfaces.

3. Results and discussion

3.1. Porosity and microstructural characterization of sintered samples

Bulk density and open porosity of sintered samples are shown in Fig. 2. While it is commonplace to plot relative density, bulk density is shown because it is not possible to differentiate between LSO phases from an XRD pattern, as we have previously discussed [26]. However, taking into account that the density of $La_{9.33}(SiO_4)_6O_2$ is 5.32 g/cm^3 according to PDF 00-049-0443 and the density of $La_{10}(SiO_4)_6O_3$ is 5.61 g/cm^3 according to PDF 00-053-0291, we can limit the relative density of the most dense material, M15, to a range between 94% and 99% of theoretical density.

It can also be seen that porosity, whose calculation is independent of the composition of the material, reaches a value of 8% at a sintering temperature of 1400 °C and of 0.25% at 1500 °C, corroborating that densification has occurred to a high degree.

3.2. Young's modulus and flexural strength

Fig. 3 shows Young's modulus measured by the impulse excitation technique (E_{IET}) related to the porosity of the samples. For E_{IET} calculation, Poisson's modulus was assumed to be 0.3; Morales et al. affirm that a rough estimate of Poisson's modulus produces a minimal uncertainty [35]. Fitting was done using functions suggested by Pabst et al. [36], namely the exponential, power law and empirical average

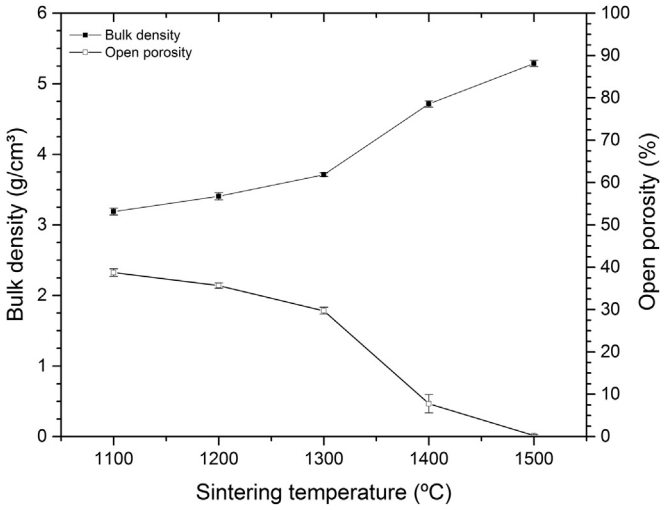

Fig. 2. bulk density and open porosity of sintered samples as a function of sintering temperature. Closed marks represent density and open marks represent porosity.

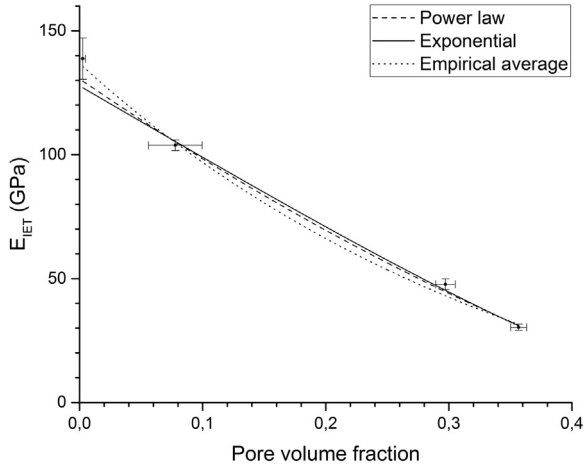

Fig. 3. Young's modulus, measured by impulse excitement technique, as a function of pore volume fraction.

functions, Eqs. (4), (5) and (6), respectively.

$$E = E_0 \exp\left(\frac{-2\Phi}{1-\Phi}\right) \quad (4)$$

$$E = E_0(1-\Phi)^2 \quad (5)$$

$$E = E_0\left[\frac{(1-\Phi)^2}{1+\Phi}\right] \quad (6)$$

where E is Young's modulus, E_0 is Young's modulus of the solid phase (i.e., a fully dense material's Young's modulus) and Φ is the porosity (volume fraction of pores). The least squares fitting of these equations give an E_0 of 144 GPa, 169 GPa and 151 GPa for the exponential, power law and empirical average functions, respectively. To the authors' knowledge, this is the first time this data is reported.

For these equations to give an adequate fitting, a negative parameter b was added to each one, which would cause the model to predict negative values of Young's modulus at higher porosities. As such, the fittings here presented should only be considered valid for a range of porosities between 0% and 40%. If high porosity LSO materials ever become of technological interest, new mechanical tests should be performed in order to investigate their behaviour.

The Young's modulus measured by nanoindentation (E_{NI}) of an M15 sample is 81.7 GPa. It can be seen that E_{NI} is lower than E_{IET}, contrary to the expected behaviour. Generally, nanoindentation analysis gives higher values, as the smaller imprints may fall entirely on a grain and thus giving local, fully dense material measurements [37].

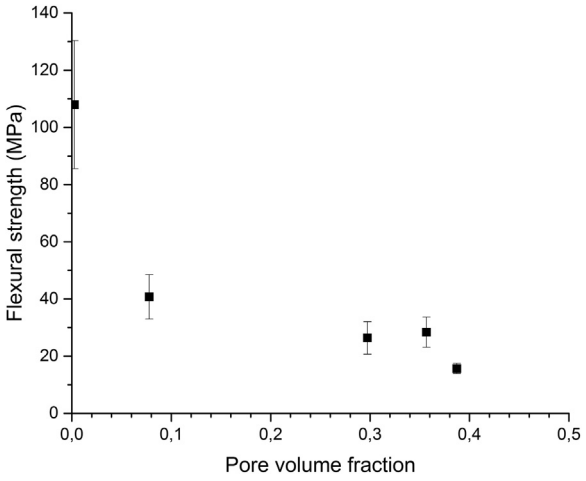

Fig. 4. flexural strength as a function of pore volume fraction.

Fig. 4 shows flexural strength related to the porosity of the samples. It can be seen that for increasing pore volume fraction, flexural strength decreases; this trend is expectable for ceramic materials where porosity is due to partial sintering. For near zero porosity, although there is a greater dispersion of data between samples, it can be seen that flexural strength reaches a mean value of 108 MPa. This could be explained by a different fracture behaviour for almost fully dense ceramics than for sub-sintered ceramics.

3.3. Hardness and fracture toughness

Fig. 5 shows Vickers hardness, HV, related to the porosity of the samples. Only three points are shown, as M12 samples were too porous to distinguish the indentation mark using the Buehler Indentamet. It can be seen that as porosity decreases due to the sinterization process, hardness increases. By extrapolation it can be calculated that full dense ceramic would have a Vickers hardness around 6 GPa, assuming similar microstructure features, such as grain size.

Fracture toughness, K_{IC}, was calculated from crack lengths developed from the vertices of indentation marks of M14 and M15 samples, as M13 samples were too porous to distinguish the cracks' path. The type of crack can be determined via the c/a ratio, where c is the crack

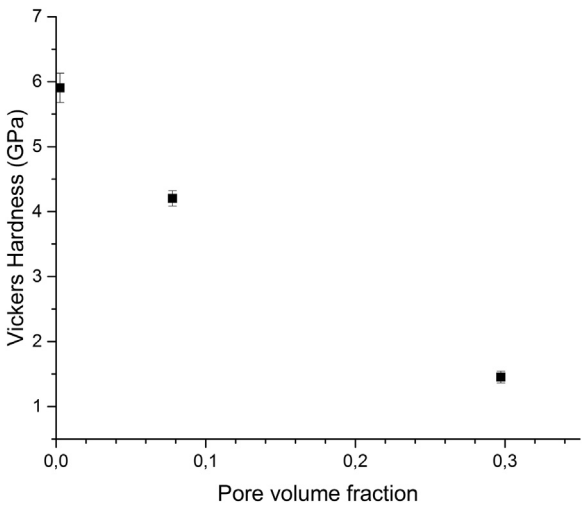

Fig. 5. Vickers hardness as a function of pore volume fraction.

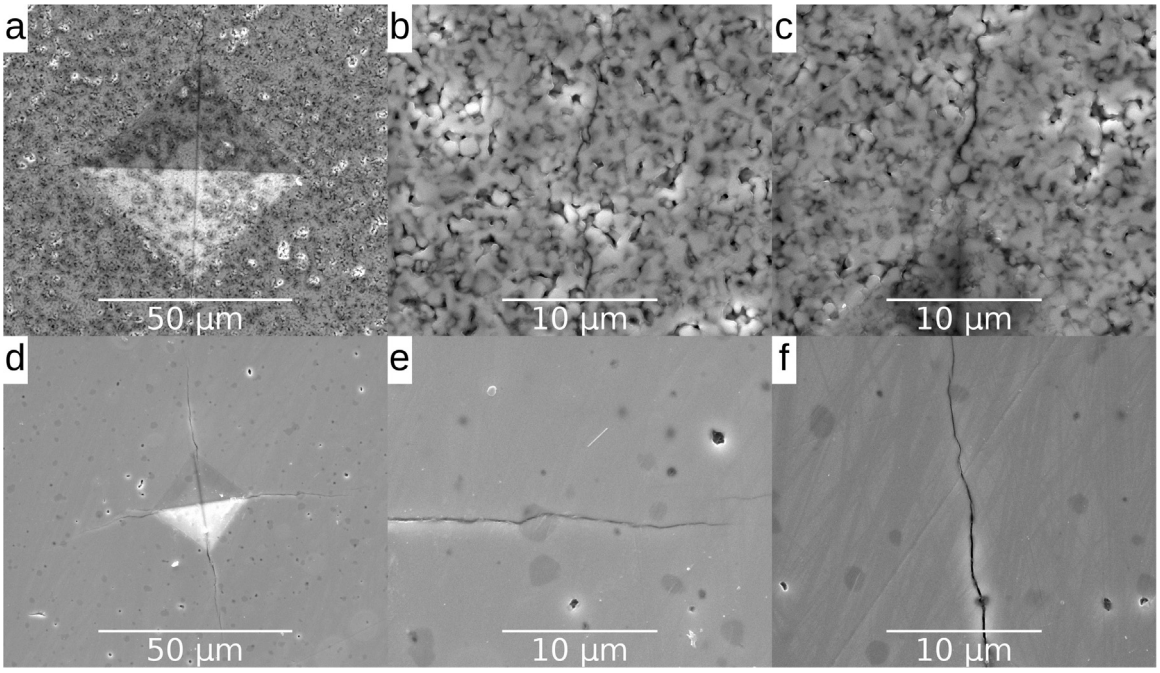

Fig. 6. SEM micrographs of an M13 sample (a, b and c) and an M15 sample (d, e and f), showing the microstructure of those materials and microhardness indentations.

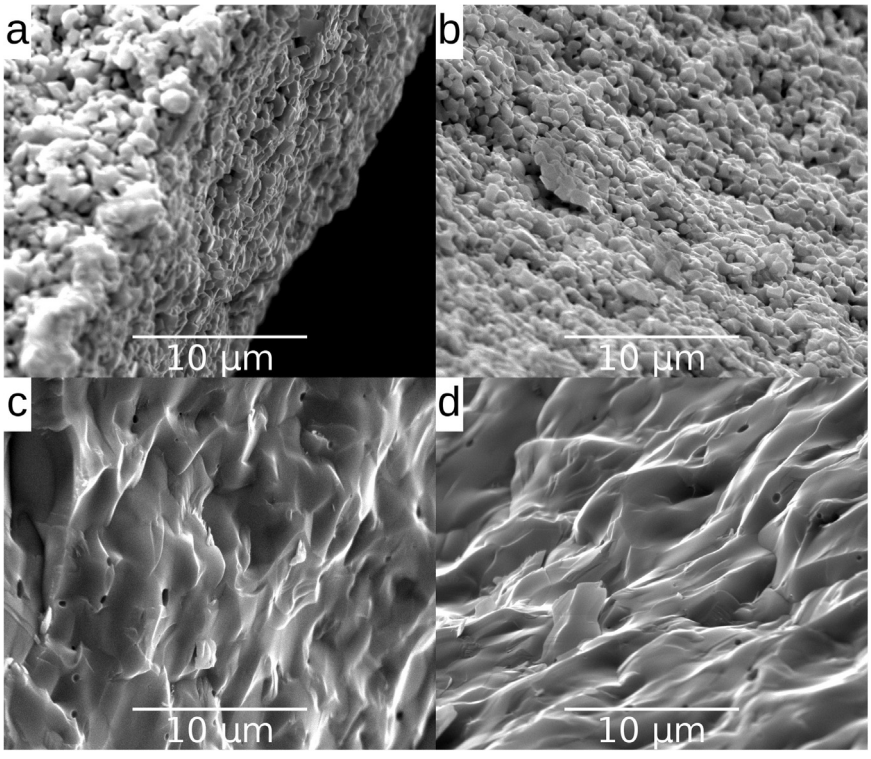

Fig. 7. SEM micrographs at the fracture surface of an M13 sample (a and b) and an M15 sample (c and d).

length and a is the indentation diagonal. c/a values lower than 2.5 correspond to Palmqvist cracks, while c/a values bigger than 2.5 indicate the presence of a median crack. c/a ratios for samples sintered at 1400 °C and 1500 °C is 2.22 and 2.81, respectively. K_{IC} is calculated using Lankford's equation [34], which has demonstrated great agreement for fitting both Palmqvist cracks and median cracks. K_{IC} of the M14 and M15 sintered samples are 1.36 and 1.18 MPa $m^{1/2}$, respectively. These values difference is expected due to the difference in the c/a ratio, as Eq. (4) decreases more rapidly with an increase in c/a ratio than it increases with an increase of E or H.

Fig. 6.a and d show SEM micrographs of the Vickers indentation of an M13 and M15 sample, respectively. It can be seen that at a sintering temperature of 1500 °C, open porosity is minimal, while at 1300 °C sintering has just begun, similarly as shown by Yang et al. [38]. In M15 samples, both indentations and cracks are easily seen, while in 1300 °C only indentations can be seen clearly: cracks hide between the greater

amount of pores. This is pronouncedly more noticeable in optical microscopy, as used in microhardness testing (Buehler Indentamet 1100); as explained before, this condition made crack lengths unmeasurable for M13.

Fig. 6.b and c show indentations and cracks evolving from their tips in the M13 sample. Fig. 6.b shows a crack developed in the M13 sample, which exhibits mainly an intergranular fracture behaviour, although some intragranular paths can be seen. Fig. 6.c shows the start of a crack at the tip of an indentation, where it can be clearly seen that intergranular fracture is the dominant path.

Fig. 6.e and f show indentations and cracks evolving from their tips in the M15 sample. Fig. 6.e shows a crack developed in the M15 sample, which exhibits a low tortuosity, indicating a primarily intragranular fracture behaviour. Fig. 6.f shows another crack developed in the M15 sample, where it can be seen that it doesn't stop at the pore. Moreover, none of the cracks finished at a pore, which indicates that pores don't have a stress releasing function.

Nanohardness (H_{NI}) of the M15 sample was of 11.79 GPa. This value is approximately two times larger than Vickers hardness for M15 sample, which is expectable due to the nature of both techniques: nanoindentation doesn't take into account grain boundaries or pores, and so is akin to a fully dense material.

3.4. Fractography

Fig. 7.a and b show SEM micrographs of the microstructure at the fracture surface of an M13 sample, while Fig. 7.c and d show SEM micrographs of the microstructure at the fracture border of an M15 sample. It can be seen that M13 microstructure has just started to from necks between grains, and that it seems that grains themselves haven't experienced a fracture process, i.e. that fracture is predominantly intergranular. M15 microstructure, in contrast, clearly presents a more dense microstructure, with only some closed pores visible and more indistinguishable grains. Grooves can be seen on the surface of grains, indicating that during fracture grains suffer from cleavage, supporting our hypothesis that the fracture mechanism is intragranular. This indicates that the grain boundaries of the samples were relatively stronger and more resistant than the grains. The fracture mechanism of the dense ceramic makes it well-suited for future SOFC applications: only under a threshold stress will the electrolyte fail catastrophically, and threshing is unexpected.

3.5. Comparison of mechanical properties between LSO and other solid oxide electrolytes

Table 1 shows mechanical properties of other SOFC electrolytes from literature. YSZ is shown due to it being currently used in commercial SOFCs. Gadolinia doped ceria (GDC) and lanthanum germanate silicate oxyapatite (LGSO) were chosen because both are good electrolytes at intermediate temperatures. In addition, LGSO is an oxyapatite similar to LSO.

It can be seen that LSO's Young's modulus is comparable to that of LGSO, but lower than that of YSZ and GDC. Most reported flexural strengths are not comparable, as only Guazzato et al. [39] uses a three-point bending as testing method; it can only be said that LSO has a lower flexural strength than that of YSZ. Regarding both Vickers hardness and nanohardness, dense LSO ceramic performs similarly to LGSO and GDC, but again YSZ shows the highest value of all considered electrolytes. The use of different equations in literature for the calculation of K_{IC} invalidates a quantitative comparison, but it can be seen that LSO behaves similarly to GDC and YSZ.

4. Conclusions

Lanthanum silicate oxyapatite (LSO, $La_{9.33+x}(SiO_4)_6O_{2+3\times/2}$; $0 < x < 0.66$), is one of encouraging materials for replacing YSZ in intermediate temperature SOFCs (IT-SOFCs). The lack of information regarding the mechanical properties of this material encourage to present a study of Young's modulus, hardness, fracture toughness and flexural strength in relation with the material's porosity. Although the present work investigates LSO mechanical behaviour for the first time, further research is needed to study this electrolyte's performance at working conditions, namely intermediate temperatures.

The least squares fitting of three equations of Young's modulus modeling curves give an E_0 of 144 GPa, 169 GPa and 151 GPa for the exponential, power law and empirical average functions, respectively. This is the first time that Young's modulus is reported for LSO.

The flexural strength measurements present a mean value for the

Table 1
summary of mechanical properties of other SOFC electrolytes (GDC, LGSO and YSZ).

Material	Reference	E_R (GPa)[a]	E_{NI} (GPa)	Flexural strength (MPa)	HV (GPa)	K_{IC} (MPa $m^{1/2}$)	H_{NI} (GPa)
GDC	Kushi et al. [40,41]	177–189					
	Morales et al. [35]		186–239[b]				10.5–16.9[k]
	Reddy et al. [42]			150–175[d]			
	Trunec [43]			144[e]			
	Fu et al. [44]				6.05[f]		
	Sato et al. [45]					1.05–1.35[i]	
LGSO	Alves et al. [46]	100–111			5.81–6.49[f]	0.97–1.20[f,i]	
	Santos et al. [23]		121		2.9–5.8[f]	3.5–3.9[f,j]	7.3–9.8
YSZ	Morales et al. [35]		223–260[b,c]				14.2–19.7[k]
	Trunec [43]			216[e]			
	Guazzato et al. [39]			680–840			
	Menvie Bekale et al. [47]				15.8[g]	1.65[g,h]	

[a] Resonance techniques, comparable to the impulse excitation method [18].
[b] For maximum loads between 5 and 500 mN.
[c] Different concentration of gadolinia dopant.
[d] Three point bending of discs.
[e] Four point bending of bars.
[f] Load of 9.8 N.
[g] Load of 0.5 N.
[h] Using Anstis equation.
[i] Using JIS R 1607 equation.
[j] Using Palmqvist equation.
[k] For maximum loads between 5 and 500 mN.

most dense samples (sintered at 1500 °C) of around 108 MPa. The full dense ceramic is expected to have a Vickers hardness around 6 GPa. Nanohardness for the most dense samples is of 11.79 GPa. SEM micrographs show that for sub-sintered materials fracture occurs via an intergranular mechanism, while for nearly full dense materials fracture behaviour is intragranular.

Acknowledgements

The authors would like to thank CONICET for the scholarship granted to RMT (166951) and to ANPCyT for the fundings (PICT 2013-1102), and Dr. Ma. Patricia Frontini and Eng. Bernardo Daga for their assistance related to nanoindentation measurements.

Declarations of interest

None.

References

[1] N. Mahato, A. Banerjee, A. Gupta, S. Omar, K. Balani, Progress in material selection for solid oxide fuel cell technology: a review, Prog. Mater. Sci. 72 (2015) 141–337, http://dx.doi.org/10.1016/j.pmatsci.2015.01.001.

[2] G. Accardo, D. Frattini, H.C. Ham, J.H. Han, S.P. Yoon, Improved microstructure and sintering temperature of bismuth nano-doped GDC powders synthesized by direct sol-gel combustion, Ceram. Int. 44 (2018) 3800–3809, http://dx.doi.org/10.1016/j.ceramint.2017.11.165.

[3] S.C. Singhal, Solid oxide fuel cells for stationary, mobile, and military applications, Solid State Ion. 152–153 (2002) 405–410, http://dx.doi.org/10.1016/S0167-2738(02)00349-1.

[4] J.M. Porras-Vázquez, E.R. Losilla, L. León-Reina, D. Marrero-López, M.A.G. Aranda, Microstructure and oxide ion conductivity in a dense $La_{9.33}$ (SiO_4)$_6O_2$ oxy-apatite, J. Am. Ceram. Soc. 92 (2009) 1062–1068, http://dx.doi.org/10.1111/j.1551-2916.2009.03032.x.

[5] B.C.H. Steele, A. Heinzel, Materials for fuel-cell technologies, Materials for Sustainability Energy, Co-Published with Macmillan Publishers Ltd, UK, 2010, pp. 224–231, , http://dx.doi.org/10.1142/9789814317665_0031.

[6] S. Nakayama, T. Kageyama, H. Aono, Y. Sadaoka, Ionic conductivity of lanthanoid silicates, Ln10(SiO4)6O3(Ln = La, Nd, Sm, Gd, Dy, Y, Ho, Er and Yb), J. Mater. Chem. 5 (1995) 1801, http://dx.doi.org/10.1039/jm9950501801.

[7] K. Kobayashi, Y. Sakka, Research progress in nondoped lanthanoid silicate oxyapatites as new oxygen-ion conductors, J. Ceram. Soc. Jpn. 122 (2014) 921–939, http://dx.doi.org/10.2109/jcersj2.122.921.

[8] P.R. Slater, J.E.H. Sansom, J.R. Tolchard, Development of apatite-type oxide ion conductors, Chem. Rec. 4 (2004) 373–384, http://dx.doi.org/10.1002/tcr.20028.

[9] S. Celerier, C. Laberty-Robert, F. Ansart, C. Calmet, P. Stevens, Synthesis by sol?Gel route of oxyapatite powders for dense ceramics: applications as electrolytes for solid oxide fuel cells, J. Eur. Ceram. Soc. 25 (2005) 2665–2668, http://dx.doi.org/10.1016/j.jeurceramsoc.2005.03.197.

[10] J.E.H. Sansom, D. Richings, P.R. Slater, Powder neutron diffraction study of the oxide-ion-conducting apatite-type phases, $La_{9.33}Si_6O_{26}$ and $La_8Sr_2Si_6O_{26}$, Solid State Ion. 139 (2001) 205–210, http://dx.doi.org/10.1016/S0167-2738(00)00835-3.

[11] L. León-Reina, E.R. Losilla, M. Martínez-Lara, S. Bruque, M.A.G. Aranda, Interstitial oxygen conduction in lanthanum oxy-apatite electrolytes, J. Mater. Chem. 14 (2004) 1142–1149, http://dx.doi.org/10.1039/B315257J.

[12] L. León-Reina, E.R. Losilla, M. Martínez-Lara, S. Bruque, A. Llobet, D.V. Sheptyakov, M.A.G. Aranda, Interstitial oxygen in oxygen-stoichiometric apatites, J. Mater. Chem. 15 (2005) 2489–2498, http://dx.doi.org/10.1039/b503374h.

[13] H. Okudera, Y. Masubuchi, S. Kikkawa, A. Yoshiasa, Structure of oxide ion-conducting lanthanum oxyapatite, $La_{9.33}(SiO_4)6O_2$, Solid State Ion. 176 (2005) 1473–1478, http://dx.doi.org/10.1016/j.ssi.2005.02.014.

[14] S. Lambert, A. Vincent, E. Bruneton, S. Beaudet-Savignat, F. Guillet, B. Minot, F. Bouree, Structural investigation of $La_{9.33}Si_6O_{26}$- and $La_9AESi_6O_26+\delta$-doped apatites-type lanthanum silicate (AE = Ba, Sr and Ca) by neutron powder diffraction, J. Solid State Chem. 179 (2006) 2602–2608, http://dx.doi.org/10.1016/j.jssc.2006.04.056.

[15] Y. Masubuchi, M. Higuchi, T. Takeda, S. Kikkawa, Preparation of apatite-type La9.33(SiO4) 6O2 oxide ion conductor by alcoxide-hydrolysis, J. Alloy. Compd. 408–412 (2006) 641–644, http://dx.doi.org/10.1016/j.jallcom.2004.12.097.

[16] H. Yoshioka, Oxide ionic conductivity of apatite-type lanthanum silicates, J. Alloy. Compd. 408–412 (2006) 649–652, http://dx.doi.org/10.1016/j.jallcom.2004.12.180.

[17] H. Zhang, Z. Li, B. Bergman, X. Zou, Investigation of $La_{9.33}Si_6O_{26}$ oxygen ionic conductor, J. Mater. Sci. Technol. 23 (2007) 629–632.

[18] Y. Nojiri, S. Tanase, M. Iwasa, H. Yoshioka, Y. Matsumura, T. Sakai, Ionic conductivity of apatite-type solid electrolyte material, La10-XBaXSi6O27-X/2 (X = 0-1), and its fuel cell performance, J. Power Sources 195 (2010) 4059–4064, http://dx.doi.org/10.1016/j.jpowsour.2010.01.050.

[19] K. Fukuda, T. Asaka, R. Hamaguchi, T. Suzuki, H. Oka, A. Berghout, E. Béchade, O. Masson, I. Julien, E. Champion, P. Thomas, Oxide-ion conductivity of highly c-axis-oriented apatite-type lanthanum silicate polycrystal formed by reactive diffusion between La_2SiO_5 and $La_2Si_2O_7$, Chem. Mater. 23 (2011) 5474–5483, http://dx.doi.org/10.1021/cm2029905.

[20] K. Fukuda, T. Asaka, S. Hara, M. Oyabu, A. Berghout, E. Béchade, O. Masson, I. Julien, P. Thomas, Crystal structure and oxide-ion conductivity along c-axis of si-deficient apatite-type lanthanum silicate, Chem. Mater. 25 (2013) 2154–2162, http://dx.doi.org/10.1021/cm400892p.

[21] A. Pons, E. Béchade, J. Jouin, M. Colas, P.-M. Geffroy, O. Masson, P. Thomas, I. Kagomiya, T. Asaka, K. Fukuda, A. Slodczyk, P. Colomban, Structural modifications of lanthanum silicate oxyapatite exposed to high water pressure, J. Eur. Ceram. Soc. 37 (2017) 2149–2158, http://dx.doi.org/10.1016/j.jeurceramsoc.2016.12.034.

[22] A. Nakajo, J. Kuebler, A. Faes, U.F. Vogt, H.J. Schindler, L.-K. Chiang, S. Modena, J. Van herle, T. Hocker, Compilation of mechanical properties for the structural analysis of solid oxide fuel cell stacks. Constitutive materials of anode-supported cells, Ceram. Int. 38 (2012) 3907–3927, http://dx.doi.org/10.1016/j.ceramint.2012.01.043.

[23] M. Santos, C. Alves, F.A.C. Oliveira, T. Marcelo, J. Mascarenhas, J.V. Fernandes, B. Trindade, Mechanical properties of sintered $La_{9.33}Si_2Ge_4O_{26}$ oxyapatite materials for SOFC electrolytes, Ceram. Int. 38 (2012) 6151–6156, http://dx.doi.org/10.1016/j.ceramint.2012.04.065.

[24] P. Vullo, M.J. Davis, Comparative study of micro-indentation and Chevron notch fracture toughness measurements of silicate and phosphate glasses, J. Non-Cryst. Solids 349 (2004) 180–184, http://dx.doi.org/10.1016/j.jnoncrysol.2004.08.181.

[25] S.P. Mukherjee, J. Zarzycki, J.M. Badie, J.P. Traverse, Influence of hydroxyl groups on the crystallization of lanthanum silicate glass, J. Non-Cryst. Solids 20 (1976) 455–458, http://dx.doi.org/10.1016/0022-3093(76)90126-5.

[26] R.J. Moreira Toja, N.M. Rendtorff, E.F. Aglietti, T. Uchikoshi, Y. Sakka, G. Suarez, Dense lanthanum silicate oxyapatite materials obtained by uniaxial pressing and slip casting, Sci. Sinter. (n.d.).

[27] K. Kobayashi, K. Hirai, T.S. Suzuki, T. Uchikoshi, T. Akashi, Y. Sakka, Sinterable powder fabrication of lanthanum silicate oxyapatite based on solid-state reaction method, J. Ceram. Soc. Jpn. 123 (2015) 274–279, http://dx.doi.org/10.2109/jcersj2.123.274.

[28] G. Pickett, Equations for computing elastic constants from flexural and torsional resonant frequencies of vibration of prisms and cylinders, Proc. Am. Soc. Test. Mater. 45 (1945) 846–865.

[29] S. Spinner, W.E. Tefft, A method for determining mechanical resonance frequencies and for calculation elastic moduli from these frequencies, Proc. ASTM 61 (1961) 1221–1238.

[30] R.C. Bradt, Elastic moduli, strength and fracture characteristics of refractories, Key Eng. Mater. 88 (1993) 165–192, http://dx.doi.org/10.4028/www.scientific.net/KEM.88.165.

[31] M. Radovic, E. Lara-Curzio, L. Riester, Comparison of different experimental techniques for determination of elastic properties of solids, Mater. Sci. Eng. A 368 (2004) 56–70, http://dx.doi.org/10.1016/j.msea.2003.09.080.

[32] W.C. Oliver, G.M. Pharr, An improved technique for determining hardness and elastic modulus using load and displacement sensing indentation experiments, J. Mater. Res. 7 (1992) 1564–1583, http://dx.doi.org/10.1557/JMR.1992.1564.

[33] P.R. Reddy, K.M. Ajith, N.K. Udayashankar, Micro and nanoindentation analysis of porous anodic alumina prepared in oxalic and sulphuric acid, Ceram. Int. 42 (2016) 17806–17813, http://dx.doi.org/10.1016/j.ceramint.2016.08.109.

[34] J. Lankford, Indentation microfracture in the Palmqvist crack regime: implications for fracture toughness evaluation by the indentation method, J. Mater. Sci. Lett. 1 (1982) 493–495, http://dx.doi.org/10.1007/BF00721938.

[35] M. Morales, J.J. Roa, X.G. Capdevila, M. Segarra, S. Piñol, Mechanical properties at the nanometer scale of GDC and YSZ used as electrolytes for solid oxide fuel cells, Acta Mater. 58 (2010) 2504–2509, http://dx.doi.org/10.1016/j.actamat.2009.12.036.

[36] Z. Živcová, M. Černý, W. Pabst, E. Gregorová, Elastic properties of porous oxide ceramics prepared using starch as a pore-forming agent, J. Eur. Ceram. Soc. 29 (2009) 2765–2771, http://dx.doi.org/10.1016/j.jeurceramsoc.2009.03.033.

[37] A.P. Silva, F. Booth, L. Garrido, E. Aglietti, P. Pena, C. Baudín, Young's modulus and hardness of multiphase CaZrO3-MgO ceramics by micro and nanoindentation, J. Eur. Ceram. Soc. 38 (2018) 2194–2201, http://dx.doi.org/10.1016/j.jeurceramsoc.2017.11.007.

[38] T. Yang, H. Zhao, J. Han, N. Xu, Y. Shen, Z. Du, J. Wang, Synthesis and densification of lanthanum silicate apatite electrolyte for intermediate temperature solid oxide fuel cell via co-precipitation method, J. Eur. Ceram. Soc. 34 (2014) 1563–1569, http://dx.doi.org/10.1016/j.jeurceramsoc.2013.12.007.

[39] M. Guazzato, M. Albakry, S.P. Ringer, M.V. Swain, Strength, fracture toughness and microstructure of a selection of all-ceramic materials, Part Ii. Zirconia-Based Dent. Ceram. Dent. Mater. 20 (2004) 449–456, http://dx.doi.org/10.1016/j.dental.2003.05.002.

[40] T. Kushi, K. Sato, A. Unemoto, S. Hashimoto, K. Amezawa, T. Kawada, Elastic modulus and internal friction of SOFC electrolytes at high temperatures under controlled atmospheres, J. Power Sources 196 (2011) 7989–7993, http://dx.doi.org/10.1016/j.jpowsour.2011.05.040.

[41] T. Kushi, K. Sato, A. Unemoto, K. Amezawa, T. Kawada, Investigation of high temperature elastic modulus and internal friction of SOFC electrolytes using resonance method, ECS (2009) 1673–1677, http://dx.doi.org/10.1149/1.3205705.

[42] K.R. Reddy, K. Karan, Sinterability, Mechanical, microstructural, and electrical properties of gadolinium-doped ceria electrolyte for low-temperature solid oxide, Fuel Cells J. Electroceram. 15 (2005) 45–56, http://dx.doi.org/10.1007/s10832-

005-1099-4.
[43] M. Trunec, Fabrication of zirconia- and ceria-based thin-wall tubes by thermoplastic extrusion, J. Eur. Ceram. Soc. 24 (2004) 645–651, http://dx.doi.org/10.1016/S0955-2219(03)00258-9.
[44] Y.-P. Fu, S.-H. Chen, J.-J. Huang, Preparation and characterization of $Ce_{0.8}M_{0.2}O_{2-\delta}$ (M = Y, Gd, Sm, Nd, La) solid electrolyte materials for solid oxide fuel cells, Int. J. Hydrog.Energy 35 (2010) 745–752, http://dx.doi.org/10.1016/j.ijhydene.2009.10.093.
[45] K. Sato, H. Yugami, T. Hashida, Effect of rare-earth oxides on fracture properties of ceria ceramics, J. Mater. Sci. 39 (2004) 5765–5770, http://dx.doi.org/10.1023/B:JMSC.0000040087.37727.cd.
[46] C. Alves, T. Marcelo, F.A.C. Oliveira, L.C. Alves, J. Mascarenhas, B. Trindade, On the influence of silica type on the structural integrity of dense $La_{9.33}Si_2Ge_4O_{26}$ electrolytes for SOFCs, J. Eur. Ceram. Soc. 33 (2013) 2251–2258, http://dx.doi.org/10.1016/j.jeurceramsoc.2012.12.024.
[47] V. Menvie Bekale, G. Sattonnay, C. Legros, A.M. Huntz, S. Poissonnet, L. Thomé, Mechanical properties of cubic zirconia irradiated with swift heavy ions, J. Nucl. Mater. 384 (2009) 70–76, http://dx.doi.org/10.1016/j.jnucmat.2008.10.007.